

5-2020


## **Parity-violating inelastic electron-proton scattering at low $Q^2$ above the resonance region**

D. Androic

David S. Armstrong

Qweak Collaboration

Follow this and additional works at: <https://scholarworks.wm.edu/aspubs>

 Part of the [Physics Commons](#)

---

## Parity-violating inelastic electron-proton scattering at low $Q^2$ above the resonance region

D. Androić,<sup>1</sup> D. S. Armstrong,<sup>2</sup> A. Asaturyan,<sup>3</sup> K. Bartlett,<sup>2</sup> R. S. Beminiwatha,<sup>4,5</sup> J. Benesch,<sup>6</sup> F. Benmokhtar,<sup>7</sup> J. Birchall,<sup>8</sup> R. D. Carlini,<sup>6,2</sup> J. C. Cornejo,<sup>2</sup> S. Covrig Dusa,<sup>6</sup> M. M. Dalton,<sup>9,6</sup> C. A. Davis,<sup>10</sup> W. Deconinck,<sup>2</sup> J. F. Dowd,<sup>2</sup> J. A. Dunne,<sup>11</sup> D. Dutta,<sup>11</sup> W. S. Duvall,<sup>12</sup> M. Elaasar,<sup>13</sup> W. R. Falk,<sup>8,\*</sup> J. M. Finn,<sup>2,\*</sup> C. Gal,<sup>9</sup> D. Gaskell,<sup>6</sup> M. T. W. Gericke,<sup>8</sup> J. Games,<sup>6</sup> V. M. Gray,<sup>2</sup> K. Grimm,<sup>5,2</sup> F. Guo,<sup>14</sup> J. R. Hoskins,<sup>2</sup> D. Jones,<sup>9</sup> M. K. Jones,<sup>6</sup> R. T. Jones,<sup>15</sup> M. Kargiantoulakis,<sup>9</sup> P. M. King,<sup>4</sup> E. Korkmaz,<sup>16</sup> S. Kowalski,<sup>14</sup> J. Leacock,<sup>12</sup> J. P. Leckey,<sup>2</sup> A. R. Lee,<sup>12</sup> J. H. Lee,<sup>2,4</sup> L. Lee,<sup>10,8</sup> S. MacEwan,<sup>8</sup> D. Mack,<sup>6</sup> J. A. Magee,<sup>2</sup> J. Mammei,<sup>12,8</sup> J. W. Martin,<sup>17</sup> M. J. McHugh,<sup>18</sup> D. Meekins,<sup>6</sup> K. E. Mesick,<sup>18,19</sup> R. Michaels,<sup>6</sup> A. Micherdzinska,<sup>18</sup> A. Mkrтчyan,<sup>3</sup> H. Mkrтчyan,<sup>3</sup> N. Morgan,<sup>12</sup> A. Narayan,<sup>11</sup> L. Z. Ndukum,<sup>11</sup> V. Nelyubin,<sup>9</sup> W. T. H. van Oers,<sup>10,8</sup> V. F. Owen,<sup>2</sup> S. A. Page,<sup>8</sup> J. Pan,<sup>8</sup> K. D. Paschke,<sup>9</sup> S. K. Phillips,<sup>20</sup> M. L. Pitt,<sup>12</sup> R. W. Radloff,<sup>4</sup> W. D. Ramsay,<sup>10,8</sup> J. Roche,<sup>4</sup> B. Sawatzky,<sup>6</sup> T. Seva,<sup>1</sup> M. H. Shabestari,<sup>11</sup> R. Silwal,<sup>9</sup> N. Simicevic,<sup>5</sup> G. R. Smith,<sup>6</sup> P. Solvignon,<sup>6,\*</sup> D. T. Spayde,<sup>21</sup> A. Subedi,<sup>11</sup> R. Suleiman,<sup>6</sup> V. Tadevosyan,<sup>3</sup> B. Waidyawansa,<sup>4</sup> P. Wang,<sup>8</sup> S. P. Wells,<sup>5</sup> S. A. Wood,<sup>6</sup> S. Yang,<sup>2</sup> and P. Zang<sup>22</sup>

(Qweak Collaboration)

<sup>1</sup>University of Zagreb, Zagreb, HR 10002, Croatia

<sup>2</sup>William & Mary, Williamsburg, Virginia 23187, USA

<sup>3</sup>A. I. Alikhanyan National Science Laboratory (Yerevan Physics Institute), Yerevan 0036, Armenia

<sup>4</sup>Ohio University, Athens, Ohio 45701, USA

<sup>5</sup>Louisiana Tech University, Ruston, Louisiana 71272, USA

<sup>6</sup>Thomas Jefferson National Accelerator Facility, Newport News, Virginia 23606, USA

<sup>7</sup>Christopher Newport University, Newport News, Virginia 23606, USA

<sup>8</sup>University of Manitoba, Winnipeg, Manitoba R3T2N2, Canada

<sup>9</sup>University of Virginia, Charlottesville, Virginia 22903, USA

<sup>10</sup>TRIUMF, Vancouver, British Columbia V6T2A3, Canada

<sup>11</sup>Mississippi State University, Mississippi State, Mississippi 39762, USA

<sup>12</sup>Virginia Polytechnic Institute & State University, Blacksburg, Virginia 24061, USA

<sup>13</sup>Southern University at New Orleans, New Orleans, Louisiana 70126, USA

<sup>14</sup>Massachusetts Institute of Technology, Cambridge, Massachusetts 02139, USA

<sup>15</sup>University of Connecticut, Storrs-Mansfield, Connecticut 06269, USA

<sup>16</sup>University of Northern British Columbia, Prince George, British Columbia V2N4Z9, Canada

<sup>17</sup>University of Winnipeg, Winnipeg, Manitoba R3B2E9, Canada

<sup>18</sup>George Washington University, Washington, DC 20052, USA

<sup>19</sup>Rutgers, the State University of New Jersey, Piscataway, New Jersey 08854, USA

<sup>20</sup>University of New Hampshire, Durham, New Hampshire 03824, USA

<sup>21</sup>Hendrix College, Conway, Arkansas 72032, USA

<sup>22</sup>Syracuse University, Syracuse, New York 13244, USA



(Received 1 November 2019; accepted 10 February 2020; published 12 May 2020)

We report the measurement of the parity-violating asymmetry for the inelastic scattering of electrons from the proton, at  $Q^2 = 0.082 \text{ GeV}^2$  and  $W = 2.23 \text{ GeV}$ , above the resonance region. The result  $A_{\text{Inel}} = -13.5 \pm 2.0(\text{stat}) \pm 3.9(\text{syst}) \text{ ppm}$  agrees with theoretical calculations, and helps to validate the modeling of the  $\gamma Z$  interference structure functions  $F_1^{\gamma Z}$  and  $F_2^{\gamma Z}$  used in those calculations, which are also used for determination of the two-boson exchange  $\gamma$ -Z box diagram ( $\square_{\gamma Z}$ ) contribution to parity-violating elastic scattering measurements. A positive parity-violating asymmetry for inclusive  $\pi^-$  production was observed, as well as positive beam-normal single-spin asymmetry for scattered electrons and a negative beam-normal single-spin asymmetry for inclusive  $\pi^-$  production.

DOI: [10.1103/PhysRevC.101.055503](https://doi.org/10.1103/PhysRevC.101.055503)

### I. MOTIVATION

The importance of two-boson exchange processes (e.g.,  $\gamma\gamma, \gamma Z$ ) to precision electromagnetic and electroweak

physics has become increasingly apparent in recent years. For example, it is now widely believed that two-photon exchange contributions can explain much (perhaps all) of the striking difference in the proton form factor ratio  $G_E^p/G_M^p$  as extracted from cross sections using the Rosenbluth separation technique and that obtained from recoil polarization measurements,

\*Deceased.

e.g., [1] (see [2] for a recent review). In electron scattering, two-photon box diagrams generate such observables as beam-normal single-spin asymmetries [3] and target-normal single-spin asymmetries [4], as well as differences between  $e^-p$  and  $e^+p$  scattering cross sections [5,6], all of which have motivated a number of experiments [7–17]. Superaligned nuclear beta-decay measurements, which are critical ingredients to tests of the unitarity of the CKM matrix, have  $\gamma W$  and  $WZ$  box diagrams as their largest nucleus-independent radiative corrections [18–20]. Theoretical control of these diagrams is therefore highly desirable [21].

A particular example of the relevance of two-boson exchange diagrams is the case of the  $\gamma Z$  box diagram in parity-violating electron scattering (PVES). In PVES, longitudinally polarized electrons scatter from an unpolarized target (a proton in the present case), and electroweak interference generates an asymmetry between the scattering cross section for right-handed ( $\sigma_R$ ) and left-handed ( $\sigma_L$ ) electrons,

$$A_{\text{PV}} = \frac{\sigma_R - \sigma_L}{\sigma_R + \sigma_L}. \quad (1)$$

Elastic PVES on the proton has been used as a powerful low-energy test of the standard model [22], because at sufficiently small four-momentum transfer, and for forward-angle scattering, this asymmetry depends in a simple way on the proton's weak charge,  $Q_W^p$ , via

$$A_{\text{PV}}/A_0 = Q_W^p + Q^2 B(Q^2, \theta), \quad A_0 = \left[ \frac{-G_F Q^2}{4\pi\alpha\sqrt{2}} \right], \quad (2)$$

where  $G_F$  is the Fermi constant,  $\alpha$  is the fine structure constant,  $-Q^2$  is the four-momentum transfer squared, and  $B(Q^2, \theta)$  encodes hadron structure effects. Within the framework of the standard model, the proton's weak charge depends in turn on the weak mixing angle,  $\theta_W$ , through the tree-level relation  $Q_W^p = 1 - 4\sin^2\theta_W$ .

Including radiative corrections, we have [23]

$$Q_W^p = (\rho + \Delta_e)(1 - 4\sin^2\theta_W(0) + \Delta'_e) + \square_{WW} + \square_{ZZ} + \square_{\gamma Z}(0), \quad (3)$$

where  $\theta_W(0)$  is the weak mixing angle at zero momentum transfer. The electroweak radiative correction terms  $\rho$ ,  $\Delta_e$ , and  $\Delta'_e$  are under good theoretical control and have been calculated to sufficient precision [23] for interpretation of existing [22] and planned [24] measurements of the weak charge. Similarly, the box diagram terms  $\square_{WW}$  and  $\square_{ZZ}$ , which are amenable to evaluation via perturbative QCD, are known to adequate precision [25]. Thus, the proton's weak charge  $Q_W^p$  is well predicted within the standard model and provides an excellent low-energy avenue to search for new physics, motivating the recent  $Q_{\text{weak}}$  [22] and future P2 [24] experiments.

This satisfactory situation was upset when Gorchtein and Horowitz [26] revealed that the  $\gamma Z$  box diagram  $\square_{\gamma Z}$  (in particular, the term  $\square_{\gamma Z}^V$ , the piece which involves the axial electron current and the vector hadron current) was strongly energy-dependent and therefore significantly larger (at the relevant beam energy scale) than had been claimed in earlier estimates [23]. They also showed that the uncertainty of  $\square_{\gamma Z}^V$

was large enough to potentially add noticeably to the projected uncertainty for the  $Q_{\text{weak}}$  measurement.

Following that initial work by Gorchtein and Horowitz, several different theoretical groups have performed calculations of the  $\square_{\gamma Z}^V$  term. Gratifyingly, there is excellent agreement on the size of  $\square_{\gamma Z}^V$  (as well as of  $\square_{\gamma Z}^A$ ) from all these calculations [27–34], although there is not yet consensus on the size of the theoretical uncertainty on  $\square_{\gamma Z}^V$ .

The most important inputs to the calculations of the  $\square_{\gamma Z}^V$  contributions are the  $\gamma Z$  interference structure functions  $F_1^{\gamma Z}$  and  $F_2^{\gamma Z}$ , which are functions of  $Q^2$  and  $W^2$  (or, equivalently,  $Q^2$  and Bjorken  $x$ ). Unfortunately, experimental input for these structure functions is scarce, unlike their purely electromagnetic analogs  $F_1^\gamma$  and  $F_2^\gamma$ . While there have been extractions of  $F_1^{\gamma Z}$  and  $F_2^{\gamma Z}$  using neutral-current deep-inelastic scattering (DIS) experiments at HERA [35], those data were at very high  $Q^2$  ( $>60 \text{ GeV}^2$ ) and small Bjorken  $x$ , while the region of the dispersion integral that is important for  $\square_{\gamma Z}^V$  calculation is high  $x$  and low  $Q^2$ . The various  $\square_{\gamma Z}^V$  calculations differ primarily in how the  $F_1^{\gamma Z}$  and  $F_2^{\gamma Z}$  were modeled in this kinematic regime, and in the uncertainties ascribed to this modeling.

This modeling of the  $\gamma Z$  interference structure functions can be tested by comparing to parity-violating electron scattering data. However, there are only two previous PVES experiments that can be used to constrain or test models of  $F_1^{\gamma Z}$  and  $F_2^{\gamma Z}$ . These are the measurements of parity-violating inelastic scattering near the  $\Delta(1232)$  resonance by the G0 Collaboration, who extracted the parity-violating asymmetry from the proton and deuteron at  $Q^2 = 0.34 \text{ GeV}^2$  and  $W = 1.18 \text{ GeV}$  [36], and the JLab Hall A E08-011 (PVDIS) Collaboration, who measured asymmetries from electron-deuteron scattering over several values of  $W$  between 1.2 to 1.98 GeV and  $Q^2$  between 0.95 and 1.47  $\text{GeV}^2$  [37]. Constraints based on the results from these two experiments were applied by the Adelaide–Jefferson Lab–Manitoba (AJM) theoretical group [32] and were important in reducing their uncertainty in  $\square_{\gamma Z}^V$ . The AJM group subsequently adopted quark-hadron duality parton distribution function (PDF) fits in order to apply additional constraints on the interference structure functions [33].

Additional experimental input to test these models of the interference structure functions, and thus test the calculation of the  $\square_{\gamma Z}^V$  diagram, would clearly be valuable; this motivated the present measurement. During a special running period of the  $Q_{\text{weak}}$  experiment [22], the beam energy was raised in order to measure the parity-violating asymmetry from the proton in an inelastic region of interest for the  $\square_{\gamma Z}^V$  calculations ( $Q^2 = 0.082 \text{ GeV}^2$  and  $W = 2.23 \text{ GeV}$ ), and for which asymmetry predictions were available using the structure function models from two of the theoretical groups (AJM [32] and Gorchtein *et al.* [28]). For this measurement the spectrometer accepted electrons and pions with a scattered momentum between 900 and 1300 MeV and an angle between  $5.8^\circ$  and  $11.6^\circ$ . For the electrons this corresponds to a range of  $Q^2$  from 0.04 to 0.15  $\text{GeV}^2$  and  $0.01 < x < 0.035$ .

In the remainder of this paper, we describe this measurement and the data analysis, and compare the extracted asymmetry to the model predictions.

## II. EXPERIMENT

The measurement was conducted using the  $Q_{\text{weak}}$  apparatus, which was located in Hall C at the Thomas Jefferson National Accelerator Facility. This apparatus was optimized for the measurement of the parity-violating asymmetry in the elastic scattering of longitudinally polarized electrons at a beam energy of 1.16 GeV from the protons in a liquid hydrogen target (the  $Q_{\text{weak}}$  weak-charge measurement [22]). A detailed discussion of the apparatus is available elsewhere [38]; here we provide an overview, followed by a presentation of those aspects that were modified for the present measurement.

The  $Q_{\text{weak}}$  apparatus was designed to detect electrons scattered from the target with scattering polar angles between  $5.8^\circ$  and  $11.6^\circ$  and 49% of  $2\pi$  in azimuth. The angular acceptance was defined by a sequence of three precision lead-alloy collimators, each with eight symmetric apertures in  $\theta$  and  $\phi$ . The azimuthal acceptances were matched to the eight open sectors (“octants”) of a toroidal spectrometer magnet. Momentum-selected scattered electrons were detected by one of eight identical fused-silica Cherenkov detectors, arranged in an azimuthally symmetric array, one detector per magnet octant. These detectors, called the main detectors (MD, numbered MD1 to MD8) were rectangular bars 2 m in length, 18 cm in width, and 1.25 cm in thickness. Cherenkov light was read out from each MD using a pair of photomultiplier tubes (PMTs), one located at each end of a given detector. Just upstream of each MD was a 2 cm thick Pb pre-radiator, which served to amplify the signal from incident electrons through generation of an electromagnetic shower and to suppress low-energy backgrounds. The main detectors were enclosed in a concrete shielding hut, with 122 cm thick walls. The upstream face of the hut was constructed of 80 cm thick high-density ( $2700 \text{ kg/m}^3$ ) concrete, loaded with barite ( $\text{BaSO}_4$ ).

In the standard mode of data-taking used for the asymmetry measurements, referred to here as “integrating mode,” the current produced by each main detector PMT was converted to a voltage and integrated during  $\approx 1$  ms long periods, known as “helicity windows,” during which the electron beam helicity was held constant (see below). The integrated PMT signal for each helicity window was then digitized and recorded.

An alternate mode, “event mode,” was used in which the beam current was reduced by six orders of magnitude (to  $\approx 0.1$  nA), and PMT signals caused by individual scattering events were read out individually and digitized. This enabled pulse-height and timing analysis of individual scattered events, which was useful for determining background fractions. During event-mode data-taking, a set of drift chambers, known as the tracking system, was inserted upstream and downstream of the magnet to track individual charged particles during dedicated periods of low-current running. This system was used for calibration purposes, background studies, and for confirmation of the kinematics and acceptance of the detected electrons.

The polarized electron-beam’s helicity was selected 960 times per second, allowing the beam to be produced in a sequence of “helicity quartets,” either  $(+ - - +)$  or  $(- + + -)$ , with the pattern chosen pseudorandomly at 240 Hz. The quartet pattern served to cancel effects due to slow linear drifts in beam properties or detector gains, while the rapid helicity reversal suppressed noise contributions due to fluctuations in either the target density or beam properties. An additional “slow” reversal of the helicity was done every 4 hours by insertion or removal of a half-wave plate in the path of the circularly-polarized laser beam used to generate the polarized electron beam.

Continuous measurements of the incident electron-beam current were made using three independent radio-frequency resonant-cavity beam current monitors (BCMs). The beam trajectory was measured using five beam-position monitors (BPMs) located upstream of the target. Energy changes were measured using another BPM at a dispersive location in the beam line.

The primary target was a high-power cryogenic liquid-hydrogen target. The hydrogen was maintained at 20 K and was contained in an aluminum-walled target cell, 34.4 cm in length, with thin Al-alloy entrance and exit windows (respectively, 0.11 and 0.13 mm thick). Several additional solid targets were available, in particular a 3.7 mm thick Al target, made of the same alloy as the hydrogen-target entrance and exit windows; the thickness of the Al target was chosen to match the radiation length of the hydrogen target.

For the present measurement, the apparatus and experimental conditions were modified in two main ways, compared to the weak-charge measurement: the beam energy was increased, and one main detector was modified to have an increased sensitivity to pions. We discuss both of these changes in the following paragraphs.

The beam energy was raised to 3.35 GeV in order to access the inelastic scattering kinematics of interest. The incident beam current was maintained between 160 and 180  $\mu\text{A}$ . Due to beam-delivery requirements for an experiment running concurrently in another experimental hall, it was not possible to deliver an electron beam which was polarized fully in the longitudinal direction. Instead, the electron spin-angle during the main data-taking, which we refer to as the “mixed” data set, was at  $\theta_p^{\text{mix}} = -19.7^\circ \pm 1.9^\circ$ , where a positive angle corresponds to an angle measured from the beam axis, rotated towards beam right in the horizontal plane. This corresponded to an electron spin with a 94.1% longitudinal component and a 33.7% (horizontal) transverse component. A beam of the same energy, but polarized almost entirely in the horizontal transverse orientation, with a polarization angle of  $\theta_p^{\text{trans}} = 92.2^\circ \pm 1.9^\circ$ , was available for part of the data-taking, which we refer to as the “transverse” data set.

The average magnitude of the polarization of the electron beam was  $P = 0.870 \pm 0.006$  for both mixed and transverse data, as measured by the Compton and Møller polarimeters [39,40] in Hall C.

Due to the higher beam energy, a significant background was present in the main detectors caused by negative pions produced in the target with momenta similar to the inelastically scattered electrons of interest. Positively charged pions

were swept out of the acceptance by the spectrometer magnetic field. With the high-rate integrating mode of detector readout, it was not possible to separate the contributions of individual electrons from individual pions to the asymmetry measurement. In order to measure and correct for this pion background, one of the main detectors (in octant 7) was modified so as to have an enhanced sensitivity to pions. The modification was the addition of a 10.2 cm thick Pb absorber ( $\approx 18$  radiation lengths), placed just upstream of the detector. This significantly attenuated the signal in this detector from scattered electrons, without affecting the signal from the majority of the  $\approx 1$  GeV pions. Thus the asymmetry in MD7 was dominated by that from incident pions, with a different mixture of electron and pion signals than in the other 7 main detectors. Under the assumption that the pion and electron fluxes were azimuthally symmetric, this difference allowed an unfolding of the separate electron and pion asymmetries. We refer to the detectors other than MD7 as “unblocked” detectors.

The mixed data set on the hydrogen target included  $9.4 \times 10^7$  helicity quartets (108 hours of data-taking), and the transverse data set included  $3.7 \times 10^6$  helicity quartets (4.3 hours of data-taking). The rate of charged particles incident on each unblocked detector was approximately 9 MHz, of which approximately 27% were pions and 73% electrons. As a typical electron produced significantly more light in an unblocked detector than did a pion, the fraction of the integrated detector signal due to pions (see Sec. III A) was 9.6%, with the remainder being mainly due to electrons. In the blocked detector, MD7, 39.7% of the integrated detector signal was due to pions, 9.3% due to electrons, and 51% due to neutral particles (see Sec. III A 3).

In order to measure the asymmetry caused by electrons scattering from the target entrance and exit windows, “mixed” data were also taken on the Al alloy target; for these runs the beam current was reduced to 60  $\mu\text{A}$ . This aluminum data set included  $5.2 \times 10^6$  helicity quartets (6.0 hours of data-taking).

### III. DATA ANALYSIS

The extraction of the parity-violating asymmetry for the inelastic scattering events took place in several steps. Event-mode data were used to determine the fraction of the experimental yield that arose due to pions and neutral particles (Sec. III A). The integrating-mode data were used to form asymmetries for each detector, and these were then corrected for several classes of false asymmetry (Sec. III B). The resulting asymmetries and yield fractions for all eight detectors were analyzed in a combined fit in order to separately extract the transverse and longitudinal asymmetries for both electrons and pions (Sec. III C). Finally, the longitudinal electron asymmetry  $A_e^L$  obtained from this fit was corrected for the effect of various backgrounds (Sec. III D) in order to obtain the inelastic parity-violating asymmetry  $A_{\text{Inel}}$ .

Each of these steps in the analysis is described in the following sections. Further details can be found in the Ph.D. thesis of one of us [41].

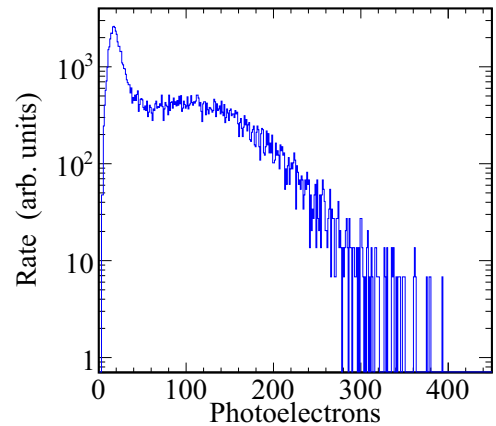


FIG. 1. Typical photoelectron spectrum, after subtraction of the electronic pedestal, for an unblocked main detector (MD4). Two distinct peaks can be seen. The narrow peak on the left, centered near 20 photoelectrons, is due to pions. The broader peak on the right, centered near 100 photoelectrons, is due to electrons.

#### A. Yield-fraction determination

Event-mode data were used to determine the fraction of the yield in the detectors that was caused by pions and by neutral particles (as opposed to the desired electrons). The existence of the Pb wall in front of the “blocked” detector (MD7) meant that these determinations were done differently for that detector compared to the seven other unblocked detectors, as discussed below.

##### 1. Pion yield-fraction in unblocked detectors

Event-mode data were used to determine  $f_\pi$ , the fraction of the pulse-height weighted signal seen in the detectors that was due to pions (or muons from their decay; these were treated together, and henceforth “pions” will refer to both). We note that negative pions can only arise in electron scattering on hydrogen through multipion production processes. There is a paucity of multipion production cross-section data available in the relevant kinematic range for this experiment, and so we relied on measured pulse-height distributions in the main detectors to determine  $f_\pi$ . Figure 1 shows a typical pulse-height spectrum in photoelectrons, for an unblocked main detector, obtained during event-mode data-taking. The spectrum is a sum of the calibrated signals of the two PMTs that read out the detector. The broad peak at larger pulse-height due to the showering electrons is clearly seen, along with the peak at lower pulse height due to the (minimum-ionizing) pions.

In order to fit these spectra to determine the fractional signal from pions and electrons, separate GEANT4 [42] simulations were generated for electrons and pions, with appropriate momenta, incident on a detector, with the generation and tracking of optical photons enabled in the simulation. These simulations provided pulse-height distributions for the two particle types. The experimental pulse-height spectra for each of the unblocked main detectors were fit to a linear combination of the simulated pion and electron spectra, with the relative fractions of the two particle types as a free parameter. The fit also included a scaling factor between photoelectrons

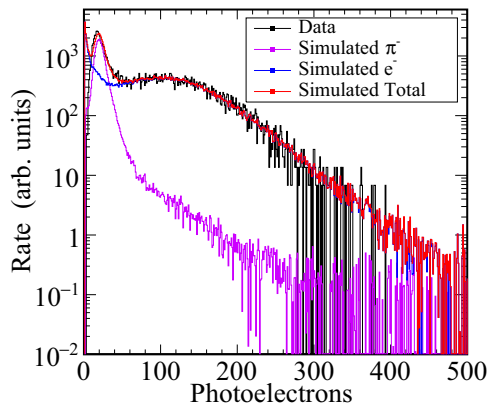


FIG. 2. Typical fit to the photoelectron spectrum from an unblocked main detector (MD4). The black histogram is the data, and the simulated spectra from pions (magenta), electrons (blue), and the sum of the electrons and pions (red) are superimposed.

(simulation) and electronic channels (data), one factor for each detector, to account for detector-to-detector variations in PMT gain. A typical fitted spectrum is shown in Fig. 2.

The pion yield fraction was calculated as

$$f_{\pi}^i = \frac{Y_{\pi}^{\text{sim}}}{Y_{\pi}^{\text{sim}} + Y_e^{\text{sim}}}, \quad (4)$$

where  $i$  is the detector number,  $Y_{\pi}^{\text{sim}}$  is the total simulated light yield from pions, and  $Y_e^{\text{sim}}$  is the total simulated light yield from electrons.

In Fig. 3, the fitted and pulse-height weighted pion-fractions for six of the eight main detectors are shown. The blocked detector MD7 was not included in this analysis, because it required a different approach to determine its pion yield fraction (see next subsection). Main detector 3 was also not included, due to a noisy PMT that distorted the pulse-height spectrum in event-mode data. The integrating-mode

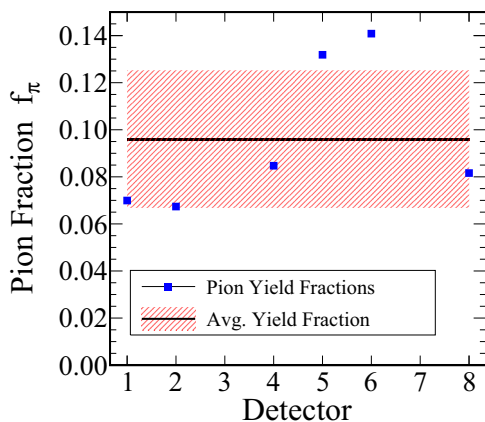


FIG. 3. The fraction of the detector yield due to pions,  $f_{\pi}^i$ , is shown for each main detector, except MD3 and MD7 (see text). The statistical uncertainties from the fitting routine are smaller than the plotting symbols. Also shown is the average value (black line) and the RMS deviation (hatched area), which we adopt as the uncertainty on the average.

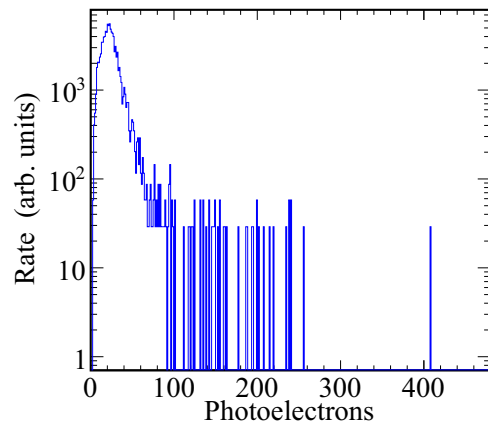


FIG. 4. Photoelectron spectrum from the blocked main detector (MD7). Only the peak due to pions ( $\approx 20$  photoelectrons) is visible; cf. Fig. 1.

asymmetry data were taken at a rate that was six orders of magnitude higher, so that this noise was negligible compared to the signal in that case. Thus, MD3 was included in the asymmetry analysis (Sec. III).

There was a significantly larger detector-to-detector variation in the pion fraction values than one would expect from statistical uncertainty alone, presumably due to an unaccounted-for systematic effect (we do not know of a physics reason for such a variation). The root-mean-squared (RMS) deviation of the six  $f_{\pi}^i$  was used as a conservative uncertainty on the average pion yield fraction to account for this systematic effect, giving a detector-averaged value of  $f_{\pi}^{\text{avg}} = 0.096 \pm 0.029$  for the unblocked detectors.

## 2. Pion yield fraction in MD7

The method described above could not be used to determine the pion yield fraction in MD7, the blocked detector, as the fraction of electrons surviving the Pb wall was so small (see Fig. 4) that the electron peak could not be reliably distinguished from the tail of the pion peak in the pulse-height spectrum. Instead, the assumption was made that both the electrons and the pions were produced with approximate azimuthal symmetry, so that the same ratio of pion flux to electron flux was incident on all eight detectors. Additional GEANT4 simulations were generated for electrons and pions, of appropriate momenta, incident on the Pb wall in MD7, to determine the signal-attenuation factors in the Pb for the electrons and pions, respectively. Applying these attenuation factors to the incident flux ratio extracted from the unblocked detectors yielded a pion light-yield fraction for MD7 of  $f_{\pi}^7 = 0.81 \pm 0.05$ .

## 3. Neutral yield fraction

The event-mode data were also used to determine the fraction of the main-detector signal which arose due to neutral particles (primarily low-energy gamma rays, but also neutrons). During this data-taking, incident charged particles could be vetoed using the plastic “trigger” scintillators from

the tracking system (for a detailed description of the tracking system, see Ref. [38]). These scintillators (218 cm long, 30 cm wide, and 1.0 cm thick), when moved into measurement position, were located just upstream of the main detectors, and covered the entire acceptance of the main detectors for particles from the target passing through the spectrometer. For the measurement of the neutral yield fraction, the data acquisition was triggered by the main-detector signal, and charged events were rejected in offline data analysis by placing cuts on the time and pulse-height spectra from the scintillators. The fraction of the yield in the unblocked main-detectors that was due to neutral particles was measured to be  $(7.8 \pm 0.4)\%$ . This was considerably larger than the  $<0.3\%$  fraction observed in the weak-charge measurement [22]. This large neutral fraction was due to several effects: (i) the contribution of “punch-through” events, in which  $\approx 3$  GeV elastically scattered electrons showered in the detector-hut shield wall, (ii) the much lower rate of inelastic electrons at the present kinematics compared to the dominant elastic electrons of the weak-charge measurement, and (iii) the “glow” of low-energy gamma rays from the interaction of very-forward scattered electrons with the beam pipe downstream of the target.

The effect of the punch-through events on the asymmetry measurement was corrected for separately (see Sec. III D 3), so here GEANT4 simulation was used to estimate the contribution of punch-through events to the neutral yield fraction. Subtracting this gives a non-punch-through neutral fraction of  $f_{\text{NB}}^{\text{Un}} = (6.3 \pm 0.6)\%$ . As this background is understood to arise mainly due to small-angle events, i.e., events at very low  $Q^2$ , it carries essentially no physics asymmetry (parity-violating asymmetries generically scale with  $Q^2$ , and parity-conserving asymmetries from two-photon exchange generically scale with  $Q$ ). We therefore treat this as a pure “dilution” to the asymmetry measurement. This background does carry a false asymmetry,  $A_{\text{BB}}$ , the correction for which is described in Sec. III B.

In the case of MD7, however, the presence of the Pb wall upstream of the detector prevented the tracking system from being moved into place to veto charged particles. Therefore, a direct measurement of the neutral yield fraction for this detector,  $f_{\text{NB}}^7$ , was not possible. Instead, an indirect method was used to infer its value. The assumption was made that the rate of the neutral events was azimuthally symmetric (i.e., that each main detector, including MD7, experienced the same neutral-particle yield). The neutral fraction in MD7 was then larger relative to the unblocked detectors due to the suppression of the charged-particle yields (electrons and pions) in the Pb wall. Again, using GEANT4 simulations to determine the suppression factors for electrons and pions due to the wall, the resulting neutral fraction was found to be  $f_{\text{NB}}^7 = (51 \pm 9)\%$ . This relatively large neutral fraction in MD7, compared to that in the unblocked detectors, arises mainly due to the factor of 70 suppression in the light yield for electrons caused by the Pb wall, and the factor of 1.6 suppression in the smaller light yield from pions. The neutral backgrounds do not arrive from the same direction as the charged particles, and are mainly not intercepted by the Pb wall, and so are largely unattenuated in MD7. Further details on the neutral-background extraction can be found in Ref. [41].

TABLE I. Asymmetries for each main detector from the mixed data set. Raw asymmetries,  $A_{\text{raw}}$ , as well as the asymmetries after correction for helicity-correlated fluctuations in beam properties,  $A_{\text{raw}} + A_{\text{beam}}$ , are shown. Note that all corrections were less than 0.20 ppm and they caused no appreciable increase in uncertainty. Note too that MD7 was blocked with a lead wall to emphasize the pion signal.

Main detector	$A_{\text{raw}}$ (ppm)	$A_{\text{raw}} + A_{\text{beam}}$ (ppm)
1	$-2.28 \pm 0.57$	$-2.24 \pm 0.57$
2	$-2.24 \pm 0.57$	$-2.24 \pm 0.57$
3	$-3.17 \pm 0.56$	$-3.19 \pm 0.56$
4	$-2.54 \pm 0.58$	$-2.58 \pm 0.58$
5	$-2.11 \pm 0.58$	$-2.10 \pm 0.58$
6	$0.35 \pm 0.58$	$0.16 \pm 0.58$
7	$1.07 \pm 0.95$	$1.07 \pm 0.95$
8	$-1.46 \pm 0.57$	$-1.49 \pm 0.57$

## B. Asymmetry determination

For integrating-mode data, the raw asymmetry as measured by a given detector was calculated, for each helicity quartet, using

$$A_{\text{raw}} = \frac{Y_+ - Y_-}{Y_+ + Y_-}. \quad (5)$$

Here  $Y_{\pm} = S_{\pm}/I_{\pm}$  is the detector yield, defined as the integrated signal from a given detector  $S_{\pm}$  (after subtraction of the electronic pedestal) normalized to the beam current  $I_{\pm}$  in each helicity window. In Eq. (5),  $Y_{\pm}$  is averaged over the two positive (negative) helicity windows in a quartet.

The raw asymmetries  $A_{\text{raw}}$  were then corrected for several sources of false asymmetry. These included (i) false asymmetries arising from helicity-correlated fluctuations in the properties (trajectory and energy) of the electron beam,  $A_{\text{beam}}$ , (ii) asymmetries arising from interactions of the electron beam with a collimator in the beamline (downstream of the target), which we refer to as the beamline background,  $A_{\text{BB}}$ , and (iii) asymmetries caused by rescattering in the preradiators upstream of each detector, which we refer to as the re-scattering bias,  $A_{\text{bias}}$ . Each of these are discussed in turn below.

(i)  $A_{\text{beam}}$ : The helicity-correlated beam correction was determined via

$$A_{\text{beam}} = - \sum_{i=1}^5 \left( \frac{\partial A}{\partial \chi_i} \right) \Delta \chi_i, \quad (6)$$

where  $\Delta \chi_i$  are the helicity-correlated differences in the trajectory or energy, as measured over a helicity quartet. The sensitivities  $\partial A/\partial \chi_i$  were determined during 6 minute intervals, using linear least-squares regression of the natural fluctuations of five beam properties: position and angle in  $x$  and  $y$ , and energy. These corrections were applied to the data for each detector, for each helicity quartet. The net result of these corrections for each detector was small, typically  $<0.05$  ppm, as detailed in Table I and Table II, and the statistical uncertainty on these corrections was negligible.

(ii)  $A_{\text{BB}}$ : In the weak-charge measurement [22], it was found that a false asymmetry arose due to secondary events

TABLE II. Asymmetries for each main detector from the transverse data set. Raw asymmetries,  $A_{\text{raw}}$ , as well as the asymmetries after correction for helicity-correlated fluctuations in beam properties,  $A_{\text{raw}} + A_{\text{beam}}$ , are shown. Note that all corrections were less than 0.15 ppm and they caused no appreciable increase in uncertainty.

Main detector	$A_{\text{raw}}$ (ppm)	$A_{\text{raw}} + A_{\text{beam}}$ (ppm)
1	$2.56 \pm 2.86$	$2.58 \pm 2.87$
2	$6.10 \pm 2.85$	$6.14 \pm 2.85$
3	$6.61 \pm 2.80$	$6.58 \pm 2.80$
4	$2.77 \pm 2.88$	$2.72 \pm 2.88$
5	$-4.56 \pm 2.90$	$-4.50 \pm 2.90$
6	$-1.07 \pm 2.88$	$-1.20 \pm 2.88$
7	$18.57 \pm 4.64$	$18.61 \pm 4.64$
8	$-3.87 \pm 2.85$	$-4.00 \pm 2.86$

scattered from the beamline and beam collimator. Such events were determined to be predominantly composed of low-energy neutral particles which contributed a small amount to the detector signal, but which carried a significant asymmetry, associated with helicity-dependent intensity and/or position fluctuations in the halo around the main accelerated electron beam. This asymmetry was monitored and corrected for, using the asymmetries measured in various auxiliary “background” detectors (see Refs. [22,43] for details). The same technique was adopted in the present analysis, resulting in only a small correction, consistent with zero:  $A_{\text{BB}} = -0.012 \pm 0.027$  ppm [41].

(iii)  $A_{\text{bias}}$ : After the polarized electrons scattered from the target, they traveled through the spectrometer’s magnetic field, causing their spins to precess. In the weak-charge measurement [22], this resulted in the initially longitudinally polarized electrons developing a significant transverse (radial) component upon reaching the main-detector array. These electrons showered and underwent multiple scattering in the Pb pradiators in front of the main detectors. The parity-conserving left-right analyzing power in the low-energy Mott scattering of the electrons from the Pb nuclei caused the asymmetries measured in the two PMTs mounted on either end of a given main detector to differ. In the weak-charge measurement, the difference between the asymmetries for the two PMTs was found to be of the order of  $A_{\text{diff}} = 0.3$  ppm. Fortunately, for perfect detector symmetry, this parity-conserving effect cancels when forming the parity-violating asymmetry of interest. Small symmetry-breaking imperfections in the main detector’s geometry and optical response functions led to a modest correction to the parity-violating asymmetry, which we refer to as the rescattering bias  $A_{\text{bias}}$ . This effect was extensively studied for the weak charge measurement [22], where the correction was found to be  $A_{\text{bias}} = 0.0043 \pm 0.0030$  ppm. The rescattering effect was also found in the present data set; the difference of the asymmetries from the two PMTs, averaged over all eight detectors, was  $A_{\text{diff}} = 1.3 \pm 0.3$  ppm. The larger physics asymmetries and larger statistical uncertainties for the present measurement meant that a similarly detailed study of  $A_{\text{bias}}$  was not required here. Instead, the previous value of  $A_{\text{bias}}$  was simply scaled by the ratio of the  $A_{\text{diff}}$  values

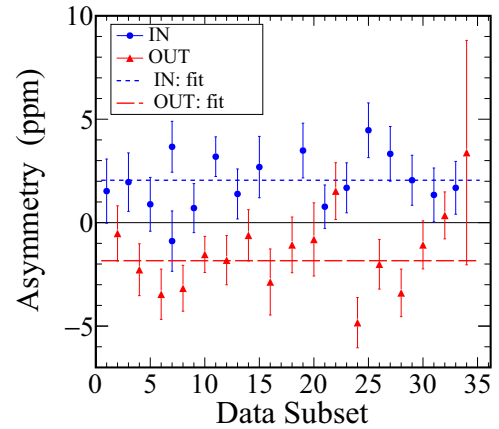


FIG. 5. Measured asymmetry from the mixed data set, averaged over the unblocked detectors, vs data subset, where each data subset corresponds to a particular state of the insertable half-wave plate used to reverse the sign of the electron-beam helicity. Each data subset represents roughly 4 hours of data-taking. The “OUT” subsets reveal the unreversed sign of the asymmetry.

between the present measurement and that from the weak-charge measurement, and, to be conservative, the uncertainty on  $A_{\text{bias}}$  was doubled, to yield  $A_{\text{bias}} = 0.019 \pm 0.028$  ppm, which is small compared to  $A_{\text{raw}}^{ij}$  (see Ref. [41] for details).

The raw asymmetries were corrected for the false asymmetries discussed above in order to generate the measured asymmetries  $A_{\text{meas}}^{ij}$  using

$$A_{\text{meas}}^{ij} = A_{\text{raw}}^{ij} + A_{\text{BB}} + A_{\text{bias}} + A_{\text{beam}}^{ij}. \quad (7)$$

Here, the index  $i = 1, 2, \dots, 8$  represents the main-detector number, and  $j$  represents the data set, either mixed or transverse. The same corrections  $A_{\text{BB}}$  and  $A_{\text{bias}}$  were used for all eight detectors. With eight main detectors and two data sets (mixed and transverse), there were sixteen total measured asymmetries  $A_{\text{meas}}^{ij}$ . The raw and measured asymmetries for the mixed data set are tabulated in Table I, and for the transverse data set in Table II.

A valuable test to ensure that false asymmetries have been properly accounted for is the behavior of the asymmetries under the “slow” reversal, wherein an insertable half-wave plate was periodically inserted into the path of the laser beam in the electron-beam source. This reversed the actual electron beam helicity with respect to the helicity signal from the source, and so should simply switch the sign of the measured asymmetry. A failure of this reversal would reveal the presence of several classes of imperfectly corrected-for false asymmetries.

The measured asymmetries were well behaved under the slow-reversal process. For example, Fig. 5 shows the average asymmetry from the seven unblocked detectors plotted vs data subset, where each data subset corresponds to a particular state of the insertable half-wave plate. The measured asymmetry reverses sign as expected; the  $p$  value for a fit of the sign-corrected asymmetries to a single value is an acceptable 0.238.



### C. Extraction of the longitudinal electron asymmetry

The measured asymmetries  $A_{\text{meas}}^{ij}$  include contributions from both scattered electrons and from pions generated in the target. For each particle type, the asymmetry includes parity-violating contributions due to the longitudinal component of the beam polarization, and parity-conserving contributions due to the transverse component of the beam polarization. These latter asymmetries, which are predominantly caused by two-photon exchange processes, vary in a sinusoidal manner with the azimuthal location of the detectors. Finally, the asymmetry measured in each detector was diluted by the fraction of the yield arising from particles other than electrons and pions, which we designate as a neutral background, as it was dominated by low-energy gamma rays.

The sign convention for a parity-conserving asymmetry from transversely polarized electrons is that the measured asymmetry varies as  $B_n \vec{P} \cdot \hat{n}$ , where  $B_n$  is the beam-normal single-spin asymmetry,  $\vec{P}$  is the electron spin-polarization vector, and  $\hat{n} = (\vec{k} \times \vec{k}') / (|\vec{k} \times \vec{k}'|)$  with  $\vec{k}(\vec{k}')$  being the momentum of the incident (scattered) electron. In the present case, the electron polarization is entirely in the horizontal plane, with positive defined as beam right. The scattered electron direction is encoded by the azimuthal angle of the given main detector,  $\phi^i$ , with  $\phi = 0^\circ$  defined as beam left, and  $\phi$  increasing in a clockwise manner. The azimuthal dependence of the asymmetry in this case reduces simply to a function of  $B_n \sin \phi^i$ .

Thus, the measured asymmetries were parametrized as

$$A_{\text{meas}}^{ij} = P(1 - f_{\text{NB}}^i) \left[ (1 - f_{\pi}^i) (A_e^L \cos \theta_p^j + A_e^T \sin \theta_p^j \sin \phi^i) + f_{\pi}^i (A_{\pi}^L \cos \theta_p^j + A_{\pi}^T \sin \theta_p^j \sin \phi^i) \right]. \quad (8)$$

Here,  $f_{\pi}^i$  is the fractional yield from pions; for MD7 this is  $f_{\pi}^7$ , and for the seven unblocked main detectors this is  $f_{\pi}^{\text{avg}}$ .  $P = 0.870 \pm 0.006$  is the total polarization of the electron beam. The longitudinal asymmetry from electrons (pions) is  $A_{e(\pi)}^L$ . The transverse asymmetry from electrons (pions) is  $A_{e(\pi)}^T$ . The beam polarization angle of data set  $j$  is  $\theta_p^j$ , with  $j = \text{“mix”}$  (mixed) or  $\text{“trans”}$  (transverse). The neutral background yield fraction for MD  $i$  is  $f_{\text{NB}}^i$ . The fixed angles corresponding to the azimuthal angle placement of the main detectors are  $\phi^i$ , with  $\phi^1 = 0^\circ$ ,  $\phi^2 = 45^\circ$ , etc.

In order to extract the four component asymmetries,  $A_e^L$ ,  $A_e^T$ ,  $A_{\pi}^L$ , and  $A_{\pi}^T$ , and their uncertainties from the measured asymmetries in Eq. (8), a Monte Carlo minimization approach was implemented. The input quantities to this minimization were  $A_{\text{meas}}^{ij}$  (see Table I),  $f_{\pi}^{\text{avg}}$  (see Sec. III A 1),  $f_{\pi}^7$  (see Sec. III A 2),  $f_{\text{NB}}^i$  (see Sec. III A 3), and  $\theta_p^j$ . A value for each input quantity was randomly selected from a Gaussian distribution about its mean with a standard deviation equal to its uncertainty. These random values were then used to calculate the asymmetry in each MD and for each polarization configuration via

$$A_{\text{calc}}^{ij} = P(1 - \tilde{f}_{\text{NB}}^i) \left[ (1 - \tilde{f}_{\pi}^i) (A_e^L \cos \tilde{\theta}_p^j + A_e^T \sin \tilde{\theta}_p^j \sin \phi^i) + \tilde{f}_{\pi}^i (A_{\pi}^L \cos \tilde{\theta}_p^j + A_{\pi}^T \sin \tilde{\theta}_p^j \sin \phi^i) \right], \quad (9)$$

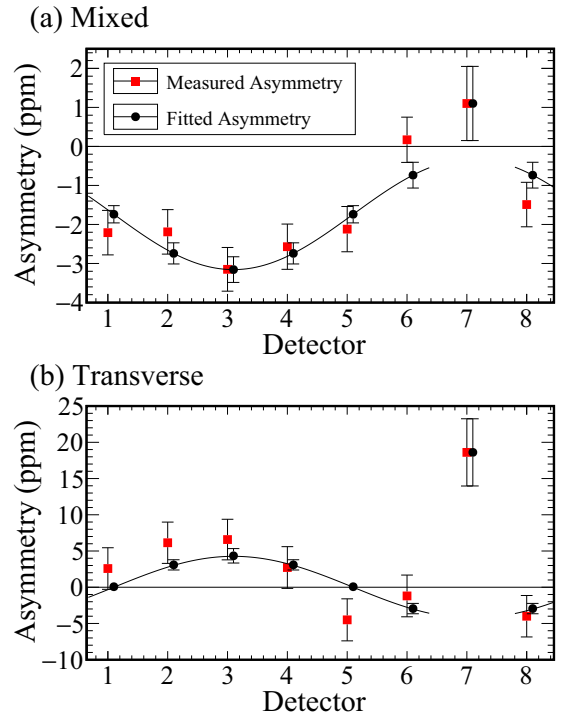


FIG. 6. Measured and fitted asymmetries vs detector number, for both (a) the mixed data set and (b) the transverse data set. The fitted data points are connected via a line to guide the eye; detector 7 is the “blocked detector” with enhanced sensitivity to pions.

where a “ $\sim$ ” over a quantity indicates a randomly selected value for that quantity. The function  $\delta$ , where

$$\delta^2 = \sum_{i,j} (\tilde{A}_{\text{meas}}^{ij} - A_{\text{calc}}^{ij})^2, \quad (10)$$

was then minimized with respect to the four unknown component asymmetries. This resulted in one possible set of values for each component asymmetry  $A_e^L$ ,  $A_e^T$ ,  $A_{\pi}^L$ , and  $A_{\pi}^T$ . The randomization and minimization process was repeated  $10^6$  times, giving  $10^6$  extracted values for each of the four component asymmetries and  $10^6$  values for the calculated asymmetries (shown in Fig. 6). Iterating  $10^6$  times ensured that each input quantity was sampled sufficiently to span its full probability distribution. This large amount of repeated input sampling also ensured that the distributions of the extracted component asymmetries varied smoothly.

The root-mean-squared (RMS) deviations of the resulting distributions are taken as the uncertainties. Correlations in the uncertainties of the extracted quantities due to the fitting are automatically accounted for in the Monte Carlo approach. The results for the four component asymmetries and their uncertainties are listed in Table III.

### D. Isolation of the parity-violating inelastic asymmetry

The asymmetry of interest  $A_{\text{Inel}}$  was contained within the longitudinal electron asymmetry,  $A_e^L$ , which was determined as described in the previous section. However  $A_e^L$  needed to be corrected for several physics backgrounds, and for the

TABLE III. Asymmetries extracted from the Monte Carlo minimization process.

Asymmetry	Value (ppm)
$A_e^L$	$-5.25 \pm 1.49$
$A_e^T$	$12.3 \pm 3.6$
$A_\pi^L$	$25.4 \pm 9.0$
$A_\pi^T$	$-60.1 \pm 19.3$

fact that the beam was not 100% polarized. There were three significant such background processes: (i) events generated by scattering in the aluminum entrance and exit windows of the target, (ii) electrons elastically scattered from the hydrogen that were radiated into the acceptance and (iii) electrons elastically scattered from the hydrogen that did not undergo radiation, but that generated signals in the detectors by ‘‘punching through’’ the concrete walls of the main detector shielding hut.

In order to correct for each of these backgrounds one needs to determine the background fraction  $f_k$ , i.e., the fraction of the signal due to background  $k$ , as well as the asymmetry due to that background,  $A_k$ . Below we discuss each of these backgrounds in turn.

### 1. Aluminum background

The fractional light-yield contribution from the aluminum target windows,  $f_{Al}$ , was estimated using GEANT4 simulation, yielding

$$f_{Al} = \frac{Y_{Al}}{Y_{Tot}} = 0.0075 \pm 0.0009, \quad (11)$$

where  $Y_{Al}$  is the yield of electrons scattered from the aluminum windows and  $Y_{Tot}$  is the total electron yield from the cryogenic target. The cross-section parametrizations used in the simulation were taken from Refs. [44,45]. The longitudinal parity-violating asymmetry from aluminum  $A_{Al}^{meas}$  was measured from dedicated runs taken on the aluminum-alloy target at the same beam energy. Consistent results for this asymmetry were measured for all eight detectors (see Fig. 7); the average value was  $A_{Al}^{meas} = -3.1 \pm 2.2$  ppm. Correcting for the beam polarization gives  $A_{Al} = A_{Al}^{meas} / (P \cos \theta_p^{mix}) = -3.8 \pm 2.7$  ppm.

This asymmetry, for the unblocked detectors, contains contributions from both electrons scattered from the aluminum as well as pions produced in the aluminum. In principle, the pion and electron asymmetries from aluminum could be separated by comparing the results for the unblocked (electron-dominated) and blocked (pion-dominated) detectors. However, there was not sufficient statistical precision in the aluminum-target data to perform such a separation; the measured blocked detector (MD7) asymmetry was identical within errors with that from the unblocked detectors (see Fig. 4). Consequently, we conservatively adopted the eight-detector average with a doubled uncertainty,  $A_{Al} = -3.8 \pm 5.4$  ppm, as our electron asymmetry from the Al windows.

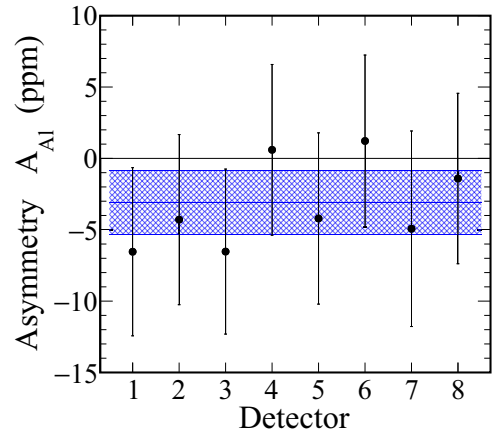


FIG. 7.  $A_{Al}$ , the asymmetry measured from the aluminum alloy target, plotted vs detector number. Errors shown are statistical only. The horizontal solid line and hatched region represent the average value and its uncertainty, respectively.

### 2. Elastic radiative tail

Elastically scattered electrons from the target, if they did not undergo radiation, were too energetic to make it cleanly into the acceptance of the spectrometer. However, if they underwent hard bremsstrahlung, either before or after the scattering vertex, they could emerge with energies ( $\approx 1.0$ – $1.2$  GeV) that allowed them into the acceptance.

The asymmetry of that fraction of the elastic radiative tail that made it into the acceptance and generated signals in the main detectors was determined using a GEANT4 simulation. Elastically scattered electrons were generated and propagated through the target and the spectrometer; the asymmetries were generated using the standard model value for the weak charge of the proton (which is consistent with our measured value [22]), and the appropriate kinematics. External bremsstrahlung processes were simulated using GEANT4 routines, and internal bremsstrahlung was accounted for following the prescription of Schwinger [46]. The acceptance-averaged asymmetry extracted from the simulation was  $A_{E1} = -0.58 \pm 0.02$  ppm.

To calculate the background fraction  $f_{E1}$  for this process, one needs to know cross sections for highly radiated elastic scattering, but also those for the inelastic scattering processes which represent our signal of interest.

For radiative processes, following Mo and Tsai [47] and Tsai [48], the angle-peaking approximation was used when calculating the angular integration of the cross sections, and the equivalent-radiator approximation was used to calculate the internal-bremsstrahlung corrections. A Coulomb correction was included following Aste *et al.* [49]. For inelastic scattering, the cross-section parametrization of Christy and Bosted [44] was adopted. The calculations of the necessary radiative corrections to the cross sections were too computationally expensive to directly embed in the GEANT4 simulation. Instead, the cross sections were calculated using an external piece of computer code originally developed by Dasu [50], and modified by a number of authors. These calculated cross sections were used to weight GEANT4 simulated events,

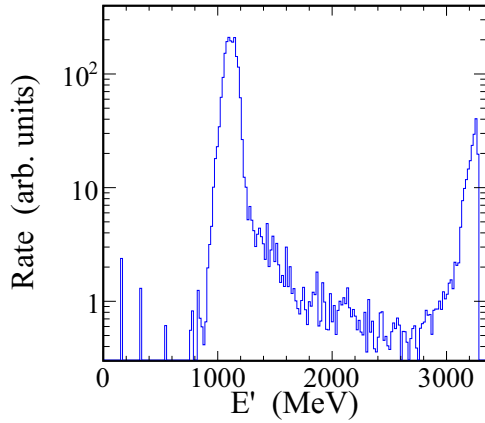


FIG. 8. Simulated energy  $E'$  spectrum for elastically scattered electrons for those events that generated signals in the main detectors (log scale). Note the two distinct peaks. The peak near 1100 MeV represents highly radiated scattered electrons that pass through the collimators and the apertures of the concrete shield hut, to directly impinge on the main detector. The peak at the right is due to elastically scattered “punch-through” electrons (see text) which had radiated little energy, but which struck the shield-hut wall, creating a shower that generated signal in the main detectors.

which thereby accounted for the experimental acceptance. The resulting elastic radiative-tail yield fraction was  $f_{\text{El}} = Y_{\text{El}}/Y_{\text{Tot}} = 0.616 \pm 0.036$ , where  $Y_{\text{El}}$  is the yield of elastically scattered electrons.

### 3. Elastic punch-through

The detector-hut shield wall was designed for the primary weak-charge measurement which had a maximum energy of scattered electrons  $E' < 1.16$  GeV. For the present measurement, with the beam energy tripled to 3.3 GeV, the copious flux of elastically scattered electrons was dumped onto the shield wall. The  $E'$  for elastic-scattering events could reach near 3.3 GeV, and thus the concrete shield wall was not thick enough to absorb all of the energy for the most energetic of these events. An additional background arose from those events which showered in the shield wall, when some of the secondaries in the shower “punched through” and deposited light in the main detectors.

To correct for this effect, GEANT4 was used to simulate elastically scattered electrons with scattered energies ranging from 150 MeV up to 3.35 GeV. Figure 8 shows the energy spectrum of scattered electrons for events for which light was deposited in one of the the main detectors. The pulse-height weighted yield fraction for these punch-through events obtained from the simulation was  $f_{\text{PT}} = Y_{\text{PT}}/Y_{\text{Tot}} = 0.0220 \pm 0.0007$ , where  $Y_{\text{PT}}$  is the yield of these punch-through events, and their asymmetry was  $A_{\text{PT}} = -3.96 \pm 0.04$  ppm.

### E. Central kinematics

A direct measurement of the central value of the four-momentum transfer for the inelastic events,  $Q_{\text{Inel}}^2$ , using the tracking system was not possible, because the inelastic events could not be distinguished experimentally from the events in

the elastic radiative tail. However, a value for  $Q_{\text{total}}^2$ , the  $Q^2$  for the predicted mixture of inelastic and radiative-tail events, was extracted from the GEANT4 simulation. This simulated value,  $Q_{\text{total(sim)}}^2 = 0.0787$  GeV<sup>2</sup> was in reasonable agreement with the experimental value from the tracking system,  $Q_{\text{total(meas)}}^2 = 0.0762$  GeV<sup>2</sup>, and the discrepancy between the two was used to estimate the uncertainties on  $Q_{\text{Inel}}^2$  and  $W$ . The resulting four-momentum transfer was  $Q_{\text{Inel}}^2 = 0.082 \pm 0.002$  GeV<sup>2</sup>, and the invariant mass  $W = 2.23 \pm 0.06$  GeV.

## IV. RESULTS

With all backgrounds having been measured or simulated, the final parity-violating asymmetry from inelastic electron-proton scattering  $A_{\text{Inel}}$  was extracted from  $A_e^L$  using

$$A_{\text{Inel}} = \frac{A_e^L - \sum_k f_k A_k}{1 - \sum_k f_k}, \quad (12)$$

where  $k = [\text{El}, \text{PT}, \text{Al}]$ , corresponding to the elastic radiative-tail, elastic punch-through, and aluminum target-window backgrounds, respectively.

This physics asymmetry was determined to be

$$\begin{aligned} A_{\text{Inel}} &= -13.5 \pm 2.0(\text{stat.}) \pm 3.9(\text{syst.}) \text{ ppm} \\ &= -13.5 \pm 4.4 \text{ ppm} \end{aligned} \quad (13)$$

at  $Q^2 = 0.082$  GeV<sup>2</sup> and  $W = 2.23$  GeV.

The uncertainty of the final  $A_{\text{Inel}}$  was dominated by systematic uncertainties (28.7% relative) (see Table IV). The four primary contributors, in decreasing order of size, were the pion yield-fractions  $f_\pi$ , the neutral background in MD7  $f_{\text{NB}}^7$ , the elastic radiative-tail yield fraction  $f_{\text{El}}$ , and the polarization angles of the electron beam  $\theta_p$ .

The present result for  $A_{\text{Inel}}$  is compared to the predictions from the AJM group [32] and from Gorchtein *et al.* [28] in Fig. 9. Our central value is larger in magnitude than that predicted by either of the two calculations; however, it agrees with both within  $1.4\sigma$  (experimental uncertainty). The relatively limited precision of the present result does not allow us to comment on the appropriateness of the somewhat smaller theoretical uncertainty quoted by the AJM group (compared to that obtained by Gorchtein *et al.*). Nonetheless, the agreement with both calculations lends confidence in the modeling of the  $F_1^{\gamma Z}$  and  $F_2^{\gamma Z}$  interference structure functions used in these calculations, which are so critical to the  $\square_{\gamma Z}$  contribution to parity-violating electron scattering.

### A. Implications of other measured asymmetries

In addition to the inelastic parity-violating asymmetry for electrons,  $A_{\text{Inel}}$ , which was the primary motivation for this measurement, three other asymmetries were obtained from fitting the data (see Table III). These were the parity-violating asymmetry for produced pions,  $A_\pi^L$ , and the transverse, or beam-normal single-spin asymmetries (BNSSA) for scattered electrons and produced pions,  $A_e^T$  and  $A_\pi^T$ , respectively.

While we did not have sufficient data available to fully correct for the physics backgrounds (elastic radiative-tail and aluminum target windows) for these observables, we can

TABLE IV. Summary of contributions to  $A_{\text{Inel}}$ , and their contributions to the uncertainty in  $A_{\text{Inel}}$ , in relative percent.

Quantity	Quantity	Value	Contribution to $\left(\frac{dA_{\text{Inel}}}{A_{\text{Inel}}}\right)$
Pion yield fraction	$f_{\pi}^{\text{avg}}$	$0.096 \pm 0.029$	21.9%
Neutral background in MD7	$f_{\pi}^7$	$0.81 \pm 0.05$	
Elastic radiative-tail yield fraction	$f_{\text{NB}}^7$	$0.51 \pm 0.09$	12.4%
Polarization angle	$f_{\text{El}}$	$0.62 \pm 0.04$	9.8%
	$\theta_p^{\text{mix}}$	$-19.7^\circ \pm 1.9^\circ$	9.3%
	$\theta_p^{\text{trans}}$	$92.2^\circ \pm 1.9^\circ$	
Neutral background in unblocked MDs	$f_{\text{NB}}^{\text{Un}}$	$0.063 \pm 0.006$	1.4%
Aluminum window asymmetry	$A_{\text{Al}}$	$-3.8 \pm 5.4$ ppm	1.0%
Beam polarization	$P$	$0.870 \pm 0.006$	0.8%
Elastic radiative tail asymmetry	$A_{\text{El}}$	$-0.58 \pm 0.02$ ppm	0.3%
Re-scattering bias effect	$A_{\text{bias}}$	$0.019 \pm 0.028$ ppm	0.2%
Aluminum window yield fraction	$f_{\text{Al}}$	$0.0075 \pm 0.0009$	0.2%
Punch-through yield fraction	$f_{\text{PT}}$	$0.0220 \pm 0.0007$	<0.1%
Beamline background asymmetry	$A_{\text{BB}}$	$0.012 \pm 0.027$ ppm	<0.1%
Punch-through asymmetry	$A_{\text{PT}}$	$-3.96 \pm 0.04$ ppm	<0.1%
Regression correction		$<0.20 \pm 0.00$ ppm	<0.1%
Total systematics			28.7%
Statistics			15.8%
Total			<b>32.8%</b>

nevertheless comment below on some implications of these asymmetries.

### 1. Electron transverse asymmetry $A_e^T$

The beam-normal single-spin asymmetry  $A_e^T$  is found to be significant and positive ( $12.3 \pm 3.6$  ppm), which is opposite in sign to all such BNSSA measured to date in *elastic* electron scattering experiments [7–11], from the proton and from complex nuclei. The aluminum window contribution to

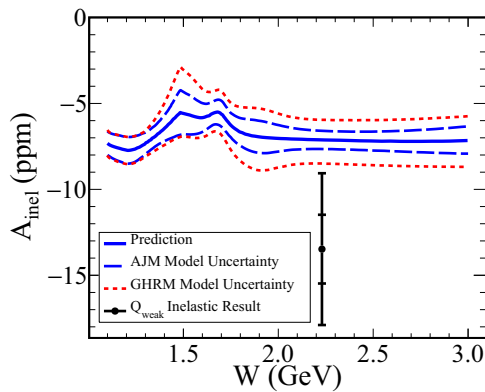


FIG. 9. Model calculations for  $A_{\text{Inel}}$  vs  $W$ , at  $Q^2 = 0.082$  GeV<sup>2</sup>, and the present measured datum (solid circle). The central values (solid curve) are from the AJM group [32] and the dashed lines represent the theoretical uncertainty from that calculation. The dotted lines are the larger theoretical uncertainties using the approach of the model by Gorchtein *et al.* [28] (adapted from Fig. 16 of Ref. [32]). The statistical (inner) and total (outer) error bars for the present measurement are indicated.

the measured  $A_e^T$  must be small, as there is no significant transverse asymmetry seen in our Aluminum-alloy target data (see Fig. 7). In order to correct for transverse asymmetries in the elastic radiative tail, one would need either BNSSA data at the appropriate kinematics or a reliable theoretical model for the BNSSA in elastic scattering from the proton. The relevant kinematics are (i) that of elastic scattering at 3.3 GeV and  $Q^2 \approx 0.21$  GeV<sup>2</sup> (for both punch-through events, Sec. III D 3, and events that radiated after the scattering vertex) and (ii) that of elastic scattering at  $\approx 1.1$  GeV and  $Q^2 \approx 0.05$  GeV<sup>2</sup> (for events that radiated before the scattering vertex). Fortunately, there are data available for the elastic BNSSA from the proton near both these kinematics. Using a 3.0 GeV beam, the G0 forward-angle transverse measurement [9] obtained  $A_e^T = -4.1 \pm 1.2$  ppm at  $Q^2 = 0.15$  GeV<sup>2</sup>, and  $A_e^T = -4.8 \pm 2.1$  ppm at  $Q^2 = 0.25$  GeV<sup>2</sup>. Our own collaboration has a preliminary elastic result of  $A_e^T = -5.5$  ppm at 1.16 GeV beam energy and  $Q^2 = 0.025$  GeV<sup>2</sup> (Ref. [51] and unpublished work). Correcting the measured  $A_e^T$  for these asymmetries, weighted by their relative contributions in a manner similar to that outlined in Sec. III D 2, leads to a crude estimate of the purely inelastic  $A_e^T$  of  $\approx +22$  ppm.

To our knowledge, there is no calculation available to date for the BNSSA for the present inelastic kinematics ( $Q^2 = 0.082$  GeV<sup>2</sup> and  $W = 2.23$  GeV), which is above the resonance region. However, Carlson *et al.* [52] have investigated the asymmetry for inelastic scattering to the  $\Delta(1232)$  resonance, at 1.16 GeV beam energy and forward scattering angle, and predicted large (40–50 ppm) positive values. That prediction is in good agreement with a preliminary result at this beam energy from our collaboration (Ref. [53] and unpublished work). The model of Carlson *et al.* included  $\Delta(1232)$ ,  $S_{11}(1535)$ , and  $D_{13}(1520)$  intermediate states in

the hadron current. We speculate that the large and positive asymmetry we have observed for inelastic scattering above the resonance region may be driven by a similar mechanism to that explored in the model of Carlson *et al.*

### 2. Pion transverse asymmetry $A_{\pi}^T$

The measured transverse asymmetry  $A_{\pi}^T = -60.1 \pm 19.3$  ppm can provide information about the BNSSA in the inclusive production of  $\pi^{-}$ 's. We did not attempt to correct the measurement for the contribution from pions produced in the aluminum. However, under the assumption that this contribution was small, and thus the signal is dominated by pions produced from the hydrogen, charge conservation dictates that we are observing multiple mesons in the final state. We are unaware of calculations appropriate to this observable. We note, however, that Buncher and Carlson have calculated the BNSSA in electron scattering in the resonance region when single final-state hadrons are observed [54]. They point out that in the case of inelastic processes in which only an outgoing pion is observed, a BNSSA can arise from single-photon exchange processes, via final-state strong interactions. The generated BNSSA can be of either sign, depending on kinematics [54].

We note that our observation of such a large ( $\approx -60$  ppm) BNSSA for inclusive pions at multi-GeV beam energies is important for the design of future precision parity-violation experiments such as the planned 11 GeV MOLLER experiment at Jefferson Lab [55], as pions might produce significant azimuthally varying background asymmetries.

### 3. Longitudinal pion asymmetry $A_{\pi}^L$

A large positive asymmetry for parity-violating inclusive  $\pi^{-}$  production,  $A_{\pi}^L = 25.4 \pm 9.0$  ppm, was extracted from the data. Again, we did not attempt to correct this for pions produced in the aluminum windows so as to extract an asymmetry for production from the proton. We can nevertheless make some comments on this result. The parity-violating asymmetry in real photoproduction should be of the order of the hadronic parity-violation parameter  $h_{\pi}^1$ , which is experimentally known to be  $(2.6 \pm 1.4) \times 10^{-7}$  [56]. The asymmetry from electroproduction of the  $\Delta(1232)$  from protons or neutrons is negative, as measured by G0 [36]. At much higher beam-energy (50 GeV), the E158 Collaboration observed a negative inclusive pion-production asymmetry of order  $-1$  ppm [57].

Explanation of the observed large *positive* asymmetry would seem to require alternative physics mechanisms. One possibility is the photoproduction (and electroproduction) of polarized hyperons,  $\Lambda$  and  $\Sigma$ . Large ( $\approx 50\%$ – $75\%$ ) transfer of polarization has been observed in electroproduction of hyperons at similar kinematics [58]. The pion-emitting weak decay (e.g.,  $\Lambda \rightarrow p\pi^{-}$ ) of such hyperons is self-analyzing, and pions emitted forward or backward in the hyperon rest frame may have different kinematic acceptances, thus leading to an asymmetry in the corresponding detection efficiency. A similar effect was seen in forward-angle parity-violating electron scattering at 3.0 GeV beam energy by the G0

Collaboration [59], who found large, positive asymmetries for protons from hyperon decay.

An alternative hypothesis is that there are large contributions from isoscalar exchange, i.e., the virtual  $Z^0$  producing multipion final states and coupling to the nucleon via isoscalar Reggeon exchange [60]. Another possible source would be pions produced in DIS at large  $W$ . There is insufficient information in the present data to distinguish between these possibilities.

Again, our observation of large ( $\approx +20$  ppm) inclusive parity-violating pion asymmetries might be relevant as a source of potential backgrounds for the MOLLER experiment [55].

## V. SUMMARY

We have measured the parity-violating asymmetry in the inelastic scattering of electrons from the proton above the resonance region, at  $Q^2 = 0.082$  GeV<sup>2</sup> and  $W = 2.23$  GeV. The result,  $A_{\text{Inel}} = -13.5 \pm 2.0(\text{stat.}) \pm 3.9(\text{syst.})$  ppm, is in acceptable agreement with two dispersion-model calculations [32] and [28]. The measurement probes the low- $Q^2$  and high- $x$  kinematic region that is most important for calculations of the  $\square_{\gamma Z}$  contribution to precision parity-violating electron-scattering measurements. The result therefore lends confidence to these calculations and to low-energy tests of the standard model that use them. However, more precise measurements would be required in order to reduce the uncertainty of the  $\square_{\gamma Z}$  calculations.

We also observed a large positive BNSSA in inelastic electron-scattering, a large negative BNSSA in the inclusive production of pions, and a large positive asymmetry in the parity-violating inclusive production of pions.

## ACKNOWLEDGMENTS

This work was supported by DOE Contract No. DEAC05-06OR23177, under which Jefferson Science Associates, LLC operates Thomas Jefferson National Accelerator Facility. Construction and operating funding for the experiment was provided through the US Department of Energy (DOE), the Natural Sciences and Engineering Research Council of Canada (NSERC), the Canadian Foundation for Innovation (CFI), and the National Science Foundation (NSF) with university matching contributions from William & Mary, Virginia Tech, George Washington University, and Louisiana Tech University. We thank the staff of Jefferson Lab, in particular the accelerator operations staff, the target and cryogenic groups, the radiation control staff, as well as the Hall C technical staff for their help and support. We are grateful for the contributions of our undergraduate students. We thank TRIUMF for its contributions to the development of the spectrometer and integrating electronics, and BATES for its contributions to the spectrometer and Compton polarimeter. We are indebted to P. G. Blunden, C. E. Carlson, M. Gorchtein, N. L. Hall, W. Melnitchouk, M. J. Ramsey-Musolf, and A. W. Thomas for many useful discussions.

- [1] A. J. R. Puckett *et al.*, *Phys. Rev. C* **96**, 055203 (2017); **98**, 019907(E) (2018).
- [2] A. Afanasev, P. G. Blunden, D. Hasell, and B. A. Raue, *Prog. Part. Nucl. Phys.* **95**, 245 (2017).
- [3] C. E. Carlson and M. Vanderhaeghen, *Annu. Rev. Nucl. Part. Sci.* **57**, 171 (2007).
- [4] O. Koshchii and A. Afanasev, *Phys. Rev. D* **98**, 056007 (2018).
- [5] P. A. M. Guichon and M. Vanderhaeghen, *Phys. Rev. Lett.* **91**, 142303 (2003).
- [6] P. G. Blunden, W. Melnitchouk, and J. A. Tjon, *Phys. Rev. Lett.* **91**, 142304 (2003).
- [7] S. P. Wells, T. Averett, D. Barkhuff, D. H. Beck, E. J. Beise, C. Benson, H. Breuer, R. Carr, S. Covrig, J. DelCorso, G. Dodson, C. Eppstein, M. Farkhondeh, B. W. Filippone, T. A. Forest, P. Frasier, R. Hasty, T. M. Ito, C. Jones, W. Korsch, S. Kowalski, P. Lee, E. Maneva, K. McCarty, R. D. McKeown, J. Mikell, B. Mueller, P. Naik, M. L. Pitt, J. Ritter, V. Savu, D. T. Spayde, M. Sullivan, R. Tieulent, E. Tsentalovich, B. Yang, and T. Zwart, *Phys. Rev. C* **63**, 064001 (2001).
- [8] F. E. Maas *et al.*, *Phys. Rev. Lett.* **94**, 082001 (2005).
- [9] D. S. Armstrong *et al.* (G0 Collaboration), *Phys. Rev. Lett.* **99**, 092301 (2007).
- [10] D. Androic *et al.* (G0 Collaboration), *Phys. Rev. Lett.* **107**, 022501 (2011).
- [11] S. Abrahamyan *et al.* (HAPPEX and PREX Collaborations), *Phys. Rev. Lett.* **109**, 192501 (2012).
- [12] D. B. Ríos, K. Aulenbacher, S. Baunack, J. Diefenbach, B. Glaser, D. vonHarrach, Y. Imai, E. M. Kabuss, R. Kothe, J. H. Lee, H. Merkel, M. C. MoraEspí, U. Müller, E. Schilling, C. Weinrich, L. Capozza, F. E. Maas, J. Arvieux, M. A. El-Yakoubi, R. Frascaria, R. Kunne, M. Morlet, S. Ong, J. van de Wiele, S. Kowalski, and Y. Prok, *Phys. Rev. Lett.* **119**, 012501 (2017).
- [13] A. Esser *et al.*, *Phys. Rev. Lett.* **121**, 022503 (2018).
- [14] I. A. Rachek *et al.*, *Phys. Rev. Lett.* **114**, 062005 (2015).
- [15] Y. W. Zhang *et al.*, *Phys. Rev. Lett.* **115**, 172502 (2015).
- [16] B. S. Henderson *et al.* (OLYMPUS Collaboration), *Phys. Rev. Lett.* **118**, 092501 (2017).
- [17] D. Rimal *et al.* (CLAS Collaboration), *Phys. Rev. C* **95**, 065201 (2017).
- [18] C.-Y. Seng, M. Gorchtein, H. H. Patel, and M. J. Ramsey-Musolf, *Phys. Rev. Lett.* **121**, 241804 (2018).
- [19] C.-Y. Seng, M. Gorchtein, and M. J. Ramsey-Musolf, *Phys. Rev. D* **100**, 013001 (2019).
- [20] M. Gorchtein, *Phys. Rev. Lett.* **123**, 042503 (2019).
- [21] C.-Y. Seng and Ulf-G. Meißner, *Phys. Rev. Lett.* **122**, 211802 (2019).
- [22] D. Androic *et al.* (Q<sub>weak</sub> Collaboration), *Nature (London)* **557**, 207 (2018).
- [23] J. Erler, A. Kurylov, and M. J. Ramsey-Musolf, *Phys. Rev. D* **68**, 016006 (2003).
- [24] D. Becker *et al.*, *Eur. Phys. J. A* **54**, 208 (2018).
- [25] M. J. Musolf and B. R. Holstein, *Phys. Lett. B* **242**, 461 (1990).
- [26] M. Gorchtein and C. J. Horowitz, *Phys. Rev. Lett.* **102**, 091806 (2009).
- [27] A. Sibirtsev, P. G. Blunden, W. Melnitchouk, and A. W. Thomas, *Phys. Rev. D* **82**, 013011 (2010).
- [28] M. Gorchtein, C. J. Horowitz, and M. J. Ramsey-Musolf, *Phys. Rev. C* **84**, 015502 (2011).
- [29] B. C. Rislow and C. E. Carlson, *Phys. Rev. D* **83**, 113007 (2011).
- [30] B. C. Rislow and C. E. Carlson, *Phys. Rev. D* **88**, 013018 (2013).
- [31] P. G. Blunden, W. Melnitchouk, and A. W. Thomas, *Phys. Rev. Lett.* **107**, 081801 (2011).
- [32] N. L. Hall, P. G. Blunden, W. Melnitchouk, A. W. Thomas, and R. D. Young, *Phys. Rev. D* **88**, 013011 (2013).
- [33] N. L. Hall, P. G. Blunden, W. Melnitchouk, A. W. Thomas, and R. D. Young, *Phys. Lett. B* **753**, 221 (2016).
- [34] J. Erler, M. Gorchtein, O. Koshchii, C.-Y. Seng, and H. Spiesberger, *Phys. Rev. D* **100**, 053007 (2019).
- [35] F. D. Aaron *et al.* (H1 Collaboration), *J. High Energy Phys.* **09** (2012) 061.
- [36] D. Androic *et al.* (G0 Collaboration), [arXiv:1212.1637](https://arxiv.org/abs/1212.1637).
- [37] D. Wang *et al.* (Jefferson Lab Hall A Collaboration), *Phys. Rev. Lett.* **111**, 082501 (2013).
- [38] T. Allison *et al.* (Q<sub>weak</sub> Collaboration), *Nucl. Instrum. Methods A* **781**, 105 (2015).
- [39] A. Narayan *et al.*, *Phys. Rev. X* **6**, 011013 (2016).
- [40] J. A. Magee *et al.*, *Phys. Lett. B* **766**, 339 (2017).
- [41] J. F. Dowd, Ph.D. thesis, College of William and Mary, 2018, [https://misportal.jlab.org/ul/publications/downloadFile.cfm?pub\\_id=15804](https://misportal.jlab.org/ul/publications/downloadFile.cfm?pub_id=15804).
- [42] S. Agostinelli *et al.*, *Nucl. Instrum. Methods A* **506**, 250 (2003).
- [43] E. Kargiantoulakis, Ph.D. thesis, University of Virginia, 2015, [https://misportal.jlab.org/ul/publications/view\\_pub.cfm?pub\\_id=14261](https://misportal.jlab.org/ul/publications/view_pub.cfm?pub_id=14261).
- [44] M. E. Christy and P. E. Bosted, *Phys. Rev. C* **81**, 055213 (2010).
- [45] P. E. Bosted and M. E. Christy, *Phys. Rev. C* **77**, 065206 (2008).
- [46] J. Schwinger, *Phys. Rev. A* **24**, 2353 (1981).
- [47] L. W. Mo and Y.-S. Tsai, *Rev. Mod. Phys.* **41**, 205 (1969).
- [48] Y.-S. Tsai, *Rev. Mod. Phys.* **46**, 815 (1974); **49**, 421(E) (1977).
- [49] A. Aste, C. von Arx, and D. Trautmann, *Eur. Phys. J. A* **26**, 167 (2005).
- [50] S. R. Dasu, Ph.D. thesis, The University of Rochester, 1988, <https://urresearch.rochester.edu/institutionalPublicationPublicView.action?institutionalItemVersionId=8058>.
- [51] B. P. Waidyawansa (Q<sub>weak</sub> Collaboration), in *11th Conference on the Intersections of Particle and Nuclear Physics (CIPANP 2012)*, 29 May–3 June 2012, St. Petersburg, FL, edited by B. Fleming, AIP Conf. Proc. No. 1560 (AIP, New York, 2013), p. 583.
- [52] C. E. Carlson, B. Pasquini, V. Pauk, and M. Vanderhaeghen, *Phys. Rev. D* **96**, 113010 (2017).
- [53] Nuruzzaman (Q<sub>weak</sub> Collaboration), in Proceedings, CIPANP 2015, [arXiv:1510.00449](https://arxiv.org/abs/1510.00449).
- [54] B. Buncher and C. E. Carlson, *Phys. Rev. D* **93**, 074032 (2016).
- [55] J. Benesch *et al.* (MOLLER Collaboration), [arXiv:1411.4088](https://arxiv.org/abs/1411.4088).
- [56] D. Blyth *et al.* (NPDGamma Collaboration), *Phys. Rev. Lett.* **121**, 242002 (2018).
- [57] P. L. Anthony *et al.* (SLAC E158 Collaboration), *Phys. Rev. Lett.* **95**, 081601 (2005).
- [58] D. S. Carman *et al.* (CLAS Collaboration), *Phys. Rev. C* **79**, 065205 (2009).
- [59] D. S. Armstrong *et al.* (G0 Collaboration), *Phys. Rev. Lett.* **95**, 092001 (2005).
- [60] M. Gorchtein (private communication).